Journal of Energy Storage 176 (2026) 123364

Contents lists available at ScienceDirect

Journal of Energy Storage

journal homepage: www.elsevier.com/locate/est

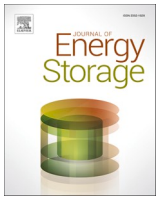

Research Papers

# Recycled concrete integration with PCM: A sustainable approach to high-efficiency latent heat thermal energy storage systems

Fardin Jafari [a,*], Matteo Dongellini [b], Giovanni Semprini [b], Gabriella Adele D'Errico [b], Alessandra Bonoli [a]

[a] Department of Civil, Chemical, Environmental and Materials Engineering, University of Bologna, Italy
[b] Department of Industrial Engineering, University of Bologna, Italy

ARTICLE INFO

*Keywords:*
Recycled concrete
PCM
Latent thermal energy storage
Experimental analysis
Thermal performance

ABSTRACT

Renewable thermal energy sources have emerged as a sustainable option to meet the heat demand for space heating and domestic hot water production in buildings. In this framework, thermal energy storage systems are crucial for optimizing the deployment of renewables. Latent Heat Thermal Energy Storage Systems (LHTESSs) using Phase Change Materials (PCMs) as a heat-storing medium offer higher energy density and reduced storage volume requirements, but face challenges due to lower heat transfer performance and cost-effectiveness. In order to enhance the storage thermal performance, metallic inserts, such as metal fins, are typically installed in these systems. However, this solution is confronted with higher fabrication and maintenance costs and corrosion.

To overcome the afore-mentioned issues, this study experimentally explores a novel LHTESS that employs a mixture of Recycled Concrete (RC) aggregate and the paraffinic PCM RT-44HC as heat-storing material. Unlike previous studies, which primarily focused on building components such as roof and ceiling tiles, this work considers the RC-PCM compound as the primary heat-storing medium in thermal energy storage systems. In order to consider different RC-PCM mixtures, RC was crushed into different grain sizes, and the thermo-physical properties of the resulting compounds were assessed. Moreover, the influence of the Heat Transfer Fluid (HTF) inlet temperature on the LHTESS thermal performance was assessed. The proposed RC-PCM compound offers a significant improvement in system thermal performance during charging and discharging cycles, up to 75%, compared to a similar storage using pure PCM as heat-storing medium. Furthermore, finer particles demonstrated approximately 10% higher heat transfer rates than coarser particles due to their lower void fraction. Additionally, the proposed solution reduces PCM usage by 55%, improving sustainability by efficiently reusing waste materials. However, the storage energy density decreases by about 40% due to the lower PCM content in the mixture compared to the pure PCM solution.

## 1. Introduction

Excessive use of fossil fuels in energy systems has raised numerous environmental issues that widely threaten human well-being. Since the building sector contributes significantly to global energy consumption to meet space heating/cooling and domestic hot water production, several researchers [1,2] have developed various platforms based on renewable energy to reduce carbon emissions over the decades. Within this framework, solar energy has gained significant attention. Solar energy primarily considers electricity generation through concentrating solar power and solar photovoltaic systems, which are applicable for heating and cooling [3]. Additionally, solar thermal systems play a crucial role in direct heat production, essential for various applications, including industrial processes and building climatization.

Renewable energy sources, such as solar energy, exhibit variable intensity due to their natural intermittence. To address these fluctuations, Thermal Energy Storage (TES) systems are essential for storing excess heat when supply exceeds demand and releasing it during nighttime or periods of low solar insolation. Generally, the TES can be classified into three categories, depending on the primary heat transfer mode: sensible, latent, and thermochemical [4]. Other factors in designing TES systems include cost, storage periods, operation conditions, and temperature requirements. Regarding heat storage media, Phase Change Materials (PCMs) significantly improve the TES storage capacity compared to conventional sensible-based TES systems, which

* Corresponding author.
*E-mail address:* fardin.jafari2@unibo.it (F. Jafari).

https://doi.org/10.1016/j.est.2026.123364
Received 10 September 2025; Received in revised form 4 June 2026; Accepted 27 June 2026
Available online 1 July 2026

**Nomenclature**

*Acronyms*

| | |
|---|---|
| HTF | Heat transfer fluid |
| LHTESS | Latent heat thermal energy storage system |
| PCM | Phase change material |
| RC | Recycled concrete |
| RP | Reference PCM |

*Greek symbols*

| | |
|---|---|
| $\alpha$ | Thermal diffusivity ($m^2/s$) |
| $\beta$ | Regression coefficient |
| $\varepsilon$ | Random error term |
| $\theta$ | Volume fraction |
| $\phi$ | Packing void fraction of recycled concrete granules (%) |
| $\rho_b$ | Bulk density of recycled concrete aggregate ($kg/m^3$) |

*Symbols*

| | |
|---|---|
| $C_p$ | Specific heat capacity (kJ/kg·K) |
| $k$ | Thermal conductivity (W/mK) |
| L | Latent heat of fusion (kJ/kg) |
| $m$ | Mass (kg) |
| $\dot{m}$ | Mass flow rate (kg/s) |
| $Nu$ | Nusselt number |
| $Pe$ | Péclet number |
| $Q$ | Thermal energy (kJ) |
| $\dot{Q}$ | Heat transfer rate (W) |
| $Re$ | Reynolds number |
| $T$ | Temperature (°C) |
| $t$ | Time (s) |
| $V$ | Volume ($cm^3$) |
| $p$ | Power density ($W/cm^3$) |

*Subscripts*

| | |
|---|---|
| $b$ | Bulk |
| $c$ | Charging |
| $con$ | Container |
| $cs$ | Concrete skeleton |
| $d$ | Discharging |
| $eff$ | Effective |
| $final$ | Final temperature |
| $in$ | Inlet |
| $initial$ | Initial temperature |
| $l$ | Liquid phase |
| $melt\_lower$ | Lower melting temperature |
| $melt\_higher$ | Higher melting temperature |
| $out$ | Outlet |
| $s$ | Solid phase |
| $sens$ | Sensible heat |
| $t$ | Total |
| $v$ | Volumetric |
| $w$ | Water |

use concrete, sand, water, and oil [5,6]. Therefore, PCMs have become pivotal materials in the TES industry due to their higher storage density, allowing a smaller system volume (and weight) [7–9].

Nowadays, several PCMs with a wide range of phase transition temperatures are available on the market. PCMs can be classified into three categories based on the phase change temperature range [9,10]:

I. Low temperature: the phase transition temperature is below 15 °C, utilized in the food industry;
II. Medium temperature: the phase transition temperature ranged between 15 and 90 °C, suitable for HVAC system applications;
III. High temperature: the phase transition is above 90 °C, primarily considered in industrial applications [11].

Various studies have attempted to improve the thermal efficiency of PCM-based storage systems. The TES efficiency can be determined by the energy storage density and the average heat transfer rate between the Heat Transfer Fluid (HTF) and storage materials [12]. Some studies focused on the impact of the HTF inlet temperature and velocity on heat transfer rate to reduce the charging and discharging cycle times. Fadl et al. [10] experimentally studied a Latent Heat Thermal Energy Storage System (LHTESS) for domestic hot water storage using paraffin RT44HC and a multi-pass vertical tube. They found that natural convection significantly enhances charging, while discharging is less affected. Increasing the flow rate from 2.5 to 7.5 l/min reduced melting time by 12–16%. Other studies investigated the impact of the PCM melting point on the heat transfer rate. For instance, Dogkas et al. [13] employed a staggered finned heat exchanger in a rectangular storage tank, filled with two organic PCMs having nominal melting temperatures of 53 °C and 58 °C. The results showed that the Sun or heat pump could charge the storage tank within 2 h when the heat transfer rate exceeded 5 kW.

Although optimizing the HTF inlet conditions enhances TES thermal performance, adding metallic fins to the heat exchanger structure is critical for improving heat transfer in PCM storage tanks. Therefore, Wang et al. [14] utilized a finned plate inside a LHTESS to reduce the charging process duration. They analyzed fins with different orientations, lengths, and thicknesses. The results revealed that heat transfer rates increased significantly with horizontal, longitudinal, and vertical fins compared to finless structures. Due to the metallic inserts, the melting time was improved by 4.52, 3.63, and 3.62 times. Zhao et al. [15] utilized fins within a rectangular enclosure to reduce the melting time of PCM. The fins were designed for vertical orientation and compared by fin length while holding the fin pitch (spacing) constant. The results revealed that a 25 mm fin requires a fin pitch of 7.5–10 mm to achieve the optimal heat transfer rate.

Several studies have investigated the effects of fin geometry on the performance of finned heat exchangers in LHTESSs. It was found that increasing the number of fins initially reduces melting time, but excessive fin density can lead to slower melting, indicating an optimal number of fins [16]. Especially under lateral or basal heating conditions, decreasing the fin spacing generally enhances the melting rate [17–19], and the optimal fin pitch can be predicted in some systems as a function of the Rayleigh number [20]. Regarding fin length, numerical and experimental studies showed that extending the fins can significantly improve melting performance, often more effectively than reducing fin spacing [21–25]. Additionally, adjusting the length ratio of upper to lower fins can optimize the melting rate, with an optimal ratio identified in specific lateral-heating systems [23]. Overall, a finer tuning of the fin arrangement, including number, spacing, and length, can significantly enhance heat transfer in LHTESSs.

On the other hand, other researchers investigated foam-based structures to increase heat transfer rates rather than using fins. For example, Meng et al. [26] used a copper foam with a high porosity of 95% and a 10 PPI pore size. Their results showed that increasing the HTF inlet temperature from 70 °C to 80 °C reduced the melting time by 42.7%. However, the cost of metal foams is much higher than that of fins, and, therefore, this solution is less suitable for practical applications.

Although utilizing metallic inserts within the storage containers or on heat exchanger tubes can provide a faster charging and discharging

process, they are not resistant to the corrosive effects of several PCMs, and their effectiveness decreases over time [27–30]. In addition, scaling up of LHTESSs with metallic inserts is complex and multiples the construction cost [31,32]. For these reasons, other heat-storing media or solutions to improve the overall system thermal performance are worth studying.

Previous works have investigated concrete and PCM composites primarily integrated in building components, like roof and ceiling tiles [33–36], rather than as the main heat storage medium. The present work addresses this gap by evaluating PCM–concrete compounds specifically as primary materials in TES systems. This study aimed to use a mixture of Recycled Concrete (RC) and PCM to develop a faster charging and discharging process without using metallic fins, thereby reducing the PCM share and associated environmental impacts and costs. The carbon emissions and cost of recycled concrete are negligible [37,38] compared to paraffin-based PCM, which generates approximately 4 kg $CO_2$/kg [39,40] and costs about 15 €/kg [41].

Specifically, the RC particles were assessed for their bulk density, chemical composition, and other relevant physical properties in this study. Then, we studied the impact of the RC grain size on the thermal performance of a LHTESS based on the commercial paraffinic PCM RT44HC during the charging and discharging processes. The results of this work can be used to design a compact, efficient, economical, and environmentally friendly LHTESS.

## 2. Methodology and experimental setup

This study is based on two experimental investigations focused on characterizing the physical and chemical properties of recycled concrete and on utilizing an RC-PCM compound as the heat-storing material within a LHTESS. Therefore, in the first part, the physical properties of RC were assessed using bulk density, packing void fraction, specific heat capacity, and SEM analysis. In the second part, three mixtures of RC-PCM were studied to assess the impact of RC properties on the LHTESS thermal performance during charging and discharging processes.

### 2.1. Recycled concrete sizing process and characterization of its physical properties

RC is selected as a granular material to mix with the PCM. The concrete was collected from train sleepers (railroad ties) and ranged in size from 5 mm to 60 mm. The concrete mix must meet high-performance standards, since it is optimized for:

- High compressive strength: typically 40–60 MPa or higher, depending on the railway application;
- Low permeability: to resist water infiltration and protect embedded reinforcement;
- High durability: to withstand freeze-thaw cycles, abrasion, and chemical attacks;
- Fatigue resistance: to endure cyclic loading from passing trains.

A typical mix design example of producing a high-quality train sleeper is listed in Table 1 [42,43].

The collected RC samples were visually inspected to ensure they were not mixed with other materials, then crushed to reduce their size. After the crushing process, the materials were sized using sieving baskets into three classes: A) 0.6–1 mm, B) 1–1.7 mm, and C) 1.7–2.36 mm. The mentioned sizing was based on the findings reported by different authors [44–47], who suggested a grain size between 0.6 and 1.7 mm. However, we added a coarser size (class C) to investigate the effect of larger particle sizes on the thermal performance and heat transfer characteristics of the LHTESS. The sizing categories are shown in Fig. 1.

**Table 1**
Components of concrete for a railway sleeper.

| Component | Proportion (by weight) |
|---|---|
| Cement (OPC or blended) | 350–450 kg/m$^3$ |
| Fine aggregates (sand) | 600–800 kg/m$^3$ |
| Coarse aggregates | 1000–1200 kg/m$^3$ |
| Water | 140–180 kg/m$^3$ |
| Admixtures | 1–2% of cement weight |

The concrete grains were washed frequently, as the dust affects the bulk density and packing void fraction test results. Then, the samples were placed in an oven at 105 °C for 1 week to dry the materials. In the next step, each sample was filled into a graduated cylinder up to 50 ml with an accuracy of ± 0.5 ml, and its weight was recorded after compaction using a vibration device. Finally, water was added to the cylinder to fill the space among the concrete grains. Each test was repeated five times to confirm repeatability. This procedure measures the packing (inter-particle) void fraction, reflecting the empty spaces between grains in the packed bed. The intra-particle porosity of the aggregate must be determined by separate saturation or pycnometer methods, and will be the object of further studies.

The bulk density ($\rho_b$) of the packed RC aggregate is calculated as [45,46]:

$$\rho_b = \frac{m_{RC}}{V_t} \tag{1}$$

where $m_{RC}$ is the mass of the recycled concrete sample, and $V_t$ is the total bulk volume of the packed sample. In this study, the packing (inter-particle) void fraction, $\phi_{pack}$, is defined as:

$$\phi_{pack} = \frac{V_w}{V_t} \times 100\% \tag{2}$$

In the previous equation, the term $V_w$ denotes the volume of water absorbed by the granules, while $V_t$ refers to the total volume of the granules.

Regarding the PCM uptake of recycled concrete particles, a gravimetric impregnation procedure was used to quantify PCM uptake by the recycled concrete (RC) particles, repeated three times. Dry RC samples (10 g) were immersed in PCM and placed in an oven at 60 °C, 16 K above the PCM melting temperature, to ensure that the PCM remained fully molten during impregnation. After 3 days, the samples were removed, excess surface PCM was carefully wiped off, and the samples were reweighed. The procedure was applied to all RC fractions (C1, C2, and C3).

The recycled concrete samples were also examined in terms of their chemical properties using MIRA3, a high-resolution scanning electron microscope (SEM). This analysis helps to understand how grain size influences the distribution of chemical components in the material. The procedure for SEM analysis using an MIRA3 device involved preparing the sample, either as a fine powder or as a solid piece, to ensure accurate analysis. Particle morphologies were examined using a TESCAN MIRA3 SEM at 140× magnification, 20 kV accelerating voltage, 14.9 mm working distance, and 1.18 μm pixel size. Elemental composition was measured using EDS with a Bruker XFlash 6|60 detector, calibrated with NIST-traceable standard reference materials. Data were acquired at ~60 s per point, with an estimated relative uncertainty of ±2%. Results are presented both qualitatively (i.e., which elements are present) and quantitatively (i.e., their amounts), allowing for comprehensive material analysis.

### 2.2. LHTESS configuration and experimental test bench

In this study, the performance of a LHTESS based on different RC-PCM compounds was assessed experimentally. The system configuration and the test bench used for experimental runs are illustrated in Fig. 2. The LHTESS consists of a rectangular metallic case measuring


**Fig. 1.** Categorization of the selected recycled concrete grain sizes: 0.6–1 mm (A), 1–1.7 mm (B), 1.7–2.36 mm (C).

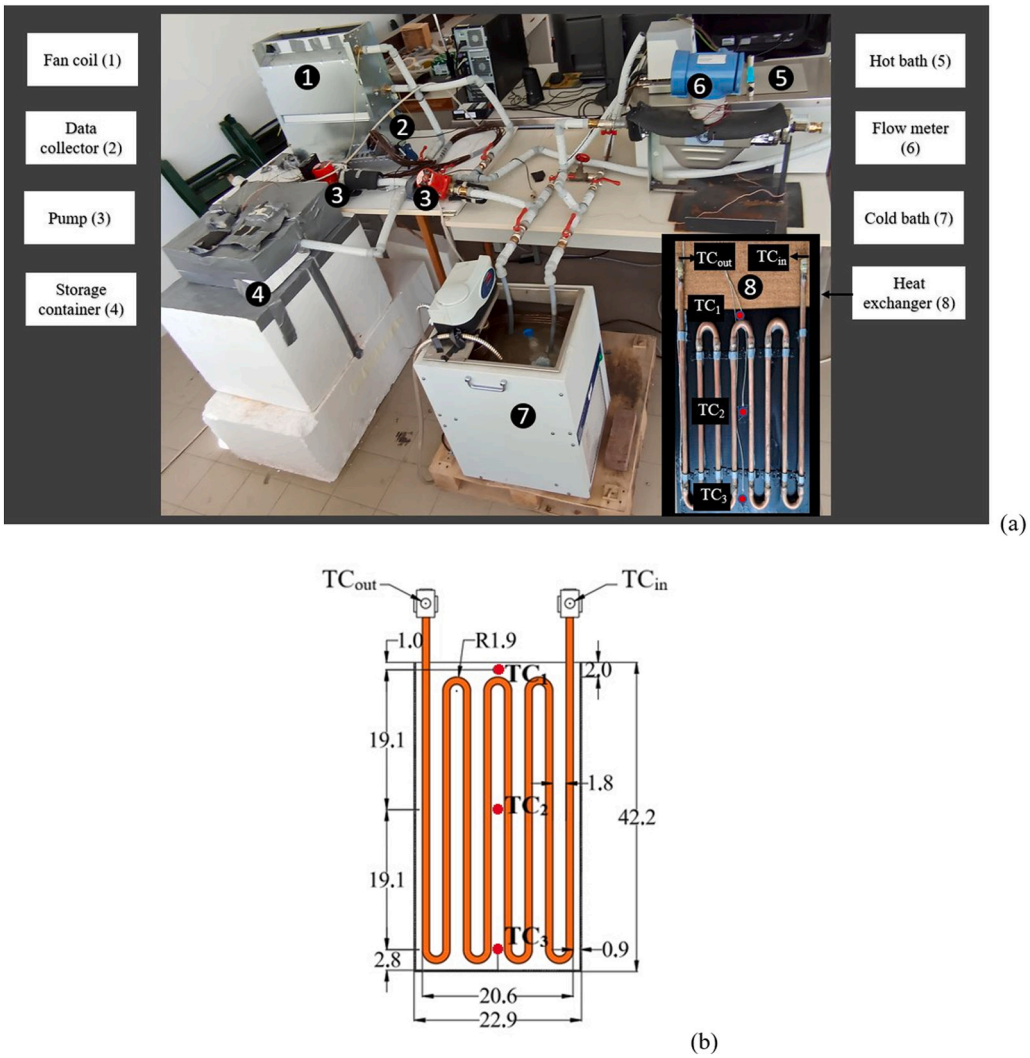


**Fig. 2.** Configuration of the LHTESS and the main components of the experimental setup (a) and schematics of the heat exchanger (all dimensions are given in centimeters) (b).

22.9·3·42.2 cm with a thickness of 2 mm, and is equipped with a vertically oriented heat exchanger made with a single-row copper tube through which the HTF flows [49]. The tube has a total length of 334 cm, an outer diameter of 1 cm, and an internal diameter of 0.87 cm. To reduce heat loss through the storage unit, a 20 cm layer of EPS insulation ($\lambda = 0.04$ W/m·K) was used to cover the LHTESS container.

Heat was stored/released in/from the LHTESS using hot and cold thermostatic baths, respectively. Pure water was used as the HTF and circulated through the system during the charging and discharging test cycles. The HTF temperature set point at the LHTESS inlet was controlled dynamically. To distribute the HTF through the TES inlet port, a series of auxiliary components, including a circulation pump

(Salmson NYL 43-25P) and flow control valves, were installed in the circuit. A Coriolis flow meter (Emerson 1700/2700 Transmitter) measured the HTF mass flow rate in the circuit with an accuracy of ±3%. The data was collected via a cDAQ device (National Instruments) and transferred to a PC every two seconds. Before filling the heat-storage material into the LHTESS, T-type thermocouples with an accuracy of ±0.2 °C were installed between the heat exchanger tubes to record the temperature of the heat-storing material. Moreover, three thermocouples were placed within the storage container. Additionally, the HTF temperature at the LHTESS inlet and outlet ports was measured using two PT1000 sensors, with an accuracy of ±0.2 °C.

To prepare the RC–PCM compounds, both the PCM and RC aggregates were heated to approximately 70 °C, well above the PCM phase change range (40–44 °C), to ensure complete PCM melting. The preheated RC aggregates were first placed in the container, and the molten PCM was then added to infiltrate the RC pore spaces. Maintaining the compound above the PCM solidification temperature range prevented subcooling effects and allowed the PCM to effectively penetrate the RC particles. This procedure was applied to produce three heat-storing materials. The weight of each material and the corresponding RC grain sizes are presented in Table 2.

The deployed RP was RT-44HC, a paraffinic material utilized frequently in previous studies on latent storage systems [51–54]. The PCM thermal and physical properties are taken from the manufacturer's data sheets and are listed in Table 3, along with the RC and container metal properties.

The effective thermal diffusivity ($\alpha_{eff}$) a fundamental property that characterizes the rate at which heat propagates through a material and is particularly important for composites containing PCMs, where transient thermal response governs performance in applications such as thermal energy storage or building envelopes. In a composite of recycled concrete aggregates (RC) and PCM, ($\alpha_{eff}$) can be estimated using its standard definition:

$$\alpha_{eff} = \frac{k_{eff}}{\rho_{eff} \times c_{p,eff}} \tag{3}$$

where $k_{eff}$ is the effective thermal conductivity, $\rho_{eff}$ is the effective density, and $c_{p,eff}$ is the effective specific heat capacity of the composite.

The effective thermal conductivity of the PCM-filled concrete was estimated using the Maxwell–Eucken model, which is suitable for composites consisting of inclusions embedded in a continuous matrix. The Maxwell–Eucken [55,56] equation adopted in this work is:

$$k_{eff} = k_{cs}\frac{k_{PCM} + 2k_{cs} - 2\theta(k_{cs} - k_{PCM})}{k_{PCM} + 2k_{cs} - \theta(k_{cs} - k_{PCM})} \tag{4}$$

where $k_{cs}$ and $k_{PCM}$ are the thermal conductivities of the concrete skeleton and PCM, respectively, and $\theta$ is the PCM volume fraction. For the present system, $\theta = 0.5447$, $k_{cs} = 2.5$ W/(m.K), and $k_{PCM} = 0.2$ W/(m.K), giving $k_{eff} = 1.04$ W/(m.K). This value is physically consistent, lying between the conductivities of the PCM and the concrete skeleton.

The effective density and specific heat were determined using the volume-weighted averaging method, also known as the Voigt model [57,58], which assumes uniform distribution and thermal equilibrium of the phases. The effective density is given by:

$$\rho_{eff} = (1-\theta)\rho_{cs} + \theta\rho_{PCM} \tag{5}$$

**Table 2**
LHTESS configurations and details on the heat-storing materials.

| LHTESS configuration | PCM mass (kg) | RC mass (kg) | RC size (mm) |
|---|---|---|---|
| RP | 1.57 | – | – |
| C1 | 0.71 | 2.7 | 0.6–1 |
| C2 | 0.71 | 2.7 | 1–1.7 |
| C3 | 0.71 | 2.7 | 1.7–2.36 |

**Table 3**
Thermophysical properties of PCM (RT-44HC), RC and metallic container.

| Property | PCM | RC | Metal |
|---|---|---|---|
| Melting range [°C] | 41–44 | – | – |
| Solidification range [°C] | 44–41 | – | – |
| Latent heat of fusion [kJ/kg] | 250 | – | – |
| Specific heat capacity [kJ/kg.K] | 2 | 0.8 | 0.4 |
| Density in solid state [kg/m$^3$] | 800 | 1450 | 6500 |
| Density in liquid state [kg/m$^3$] | 700 | – | – |
| Thermal conductivity [W/(m.K)] | 0.2 | 0.172 | 25 |
| Volume expansion [%] | 12.5 | – | – |

and the effective specific heat capacity by:

$$c_{p,eff} = (1-\theta)c_{p,cs} + \theta c_{p,PCM} \tag{6}$$

where $\rho_{cs}$ and $c_{p,cs}$ are the density and specific heat capacity of the concrete skeleton, and $\rho_{PCM}$ and $c_{p,PCM}$ are those of PCM. For the liquid PCM ($\rho_{PCM} = 700$ kg/m$^3$, $c_{p,PCM} = 2.0$ kJ/kg·K) and concrete skeleton ($\rho_{cs} = 1450$ kg/m$^3$, $c_{p,cs} = 0.8$ kJ/kg·K) the effective properties were ($\rho_{eff} \approx 1041$ kg/m$^3$,$cp_{eff} \approx 1.454$ kJ/kg·K).

Substituting these values into the thermal diffusivity definition yields $\alpha_{eff} \approx 6.87 \times 10^{-7}$ m$^2$/s for RC-PCM. This value lies between the thermal diffusivities of PCM and the concrete skeleton, reflecting the influence of low-conductivity PCM while the continuous concrete matrix maintains higher heat transfer. For comparison, pure PCM has $\alpha_{PCM} \approx 1.43 \times 1^{-7}$ m$^2$/s. Thus, the inclusion of the concrete skeleton increases the effective thermal diffusivity, thereby enhancing heat transfer within the RC-PCM compound.

### 2.3. The charging and discharging process

In this study, a closed loop was considered for both charging and discharging cycles. Fig. 3 shows the configuration of the experimental setup and the HTF stream path for the processes. The experimental tests were performed with two HTF inlet temperatures during both charging and discharging processes, with a fixed mass flow rate of 50 kg/h [59]. Based on the tube inner diameter, total length, and water properties at the mean bulk temperature, the Reynolds number ($Re$) was ≈ 3100, indicating transitional flow. The corresponding Péclet number ($Pe$) was ≈ 13,400, and the Nusselt number ($Nu$), estimated using the Dittus–Boelter correlation [60], was ≈ 58. These values show that HTF-side convection was moderate and consistent across all experiments, providing a baseline for interpreting differences in thermal performance between the RC–PCM mixtures. In addition, each measurement under identical conditions was independently repeated five times to assess experimental repeatability; these repetitions do not represent cycling or durability tests. In the charging cycle, hot water from a hot bath was circulated through the LHTESS. Heat was transferred from the HTF to the heat-storing material through the heat exchanger. The cooled HTF returned to the hot bath for reheating, ensuring continuous energy circulation.

The HTF stream absorbed heat from the storage material during the discharging process. A fan coil was used to assist in dissipating heat to the environment, preventing overheating. The HTF stream was then directed towards the cold bath. In Table 4, the temperature difference between the HTF inlet temperature and the edges of the PCM phase change range (i.e., 44 °C and 41 °C for charging and discharging processes, respectively) is denoted as $\Delta T$. The HTF operating conditions are reported in Table 4.

### 2.4. Calculation methods for the LHTESS thermal performance

The amount of net stored and released thermal energy is calculated based on an energy balance on the HTF side. The instantaneous heat transfer rate between the HTF and heat-storing material during the

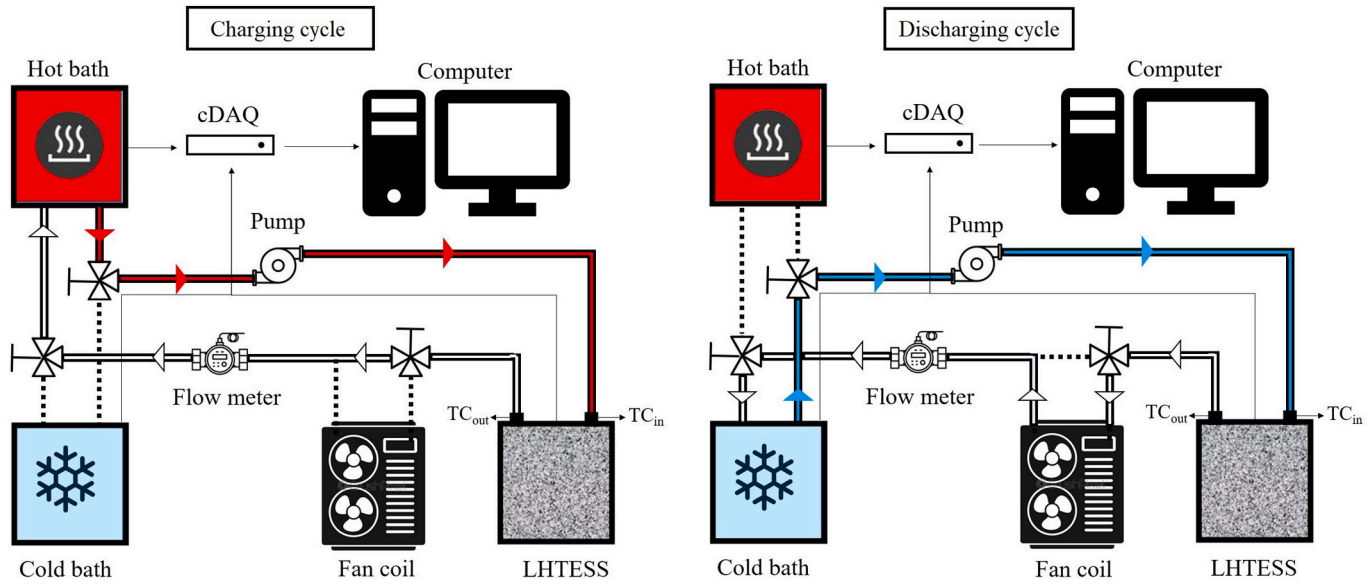


**Fig. 3.** Scheme of charging (left) and discharging (right) processes.

**Table 4**
Operating conditions of the HTF stream during the experimental tests.

| Process | HTF inlet temperature (°C) | HTF flow rate (kg/h) |
|---|---|---|
| Charging | 54 ($\Delta T = 10$ K) | 50 |
| | 59 ($\Delta T = 15$ K) | 50 |
| Discharging | 25 ($\Delta T = 15$ K) | 50 |
| | 30 ($\Delta T = 10$ K) | 50 |

charging/discharging processes ($Q_{c/d}$, respectively) can be calculated according to the following equations:

$$\dot{Q}_c = \dot{m}_{HTF} C_{p,HTF} (T_{in} - T_{out}) \tag{7}$$

$$\dot{Q}_d = \dot{m}_{HTF} C_{p,HTF} (T_{out} - T_{in}) \tag{8}$$

where $\dot{m}_{HTF}$ represents the HTF mass flow rate, $C_{p,HTF}$ is the HTF specific heat capacity, calculated for the mean temperature of the fluid, and $T_{in}$ and $T_{out}$ denote the HTF temperature at the inlet and outlet ports, respectively.

The thermocouple TC3 was selected as the evaluation point to assess the LHTESS thermal performance (see Fig. 2 for reference) due to its central position within the system. Therefore, the duration of the charging and discharging processes was calculated based on the temperature values recorded by TC3. First, the charging process is considered to begin and end when the PCM temperature measured by TC3 rises above 36 °C and 48 °C, respectively. Conversely, the discharging process begins when the TC3 records a PCM temperature below 48 °C and ends when TC3 measures a PCM temperature below 36 °C. The corresponding time instants, $t_{start,c}$, $t_{end,c}$, $t_{start,d}$, and $t_{end,d}$, denote the start and end of the charging and discharging phases, respectively.

The total thermal energy transferred during charging ($Q_c$) and discharging ($Q_d$) processes was then obtained by integrating the respective instantaneous heat transfer rates over the process durations according to Eqs. (9) and (10):

$$Q_c = \int_{t_{start,c}}^{t_{end,c}} \dot{Q}_c dt \tag{9}$$

$$Q_d = \int_{t_{start,d}}^{t_{end,d}} \dot{Q}_d dt \tag{10}$$

However, only a portion of the thermal energy exchanged between the LHTESS and HTF during the charging and discharging processes can be effectively absorbed/released by the thermal storage medium, including both the heat-storing material and the metallic case. The remaining amount of supplied/released heat can be considered a heat loss.

In order to quantify these losses during the charging process ($Q_{c,loss}$), the theoretical net heat-storage capability of the LHTESS ($Q_{c,th}$) was calculated. It is worth mentioning that this calculation was carried out in full consistency with the PCM temperature trend measured at TC3. For the charging process, the sensible heat transfer in both the solid and liquid phase and the latent heat transfer were evaluated according to the manufacturer's technical data (i.e., sensible heat transfer in the solid phase from 36 °C to 41 °C, latent heat transfer from 41 °C to 44 °C, and sensible heat transfer in the liquid phase from 44 °C to 48 °C). $Q_{c,loss}$ can be assessed according to Eqs. (11)–(18).

$$Q_{c,loss} = Q_c - Q_{c,th} \tag{11}$$

$$Q_{c,th} = \begin{cases} Q_{c,PCM} + Q_{c,cont} & \text{for configuration RP} \\ Q_{c,PCM} + Q_{c,RC} + Q_{c,cont} & \text{for configurations C1, C2, C3} \end{cases} \tag{12}$$

$$Q_{c,PCM} = Q_{sens,c,s} + Q_{lat} + Q_{sens,c,l} \tag{13}$$

$$Q_{sens,c,s} = m_{PCM} C_{p,PCM} (T_{melt,lower} - T_{initial}) \tag{14}$$

$$Q_{lat} = m_{PCM} L_{PCM} \tag{15}$$

$$Q_{sens,c,l} = m_{PCM} C_{p,PCM} (T_{final} - T_{melt,higher}) \tag{16}$$

$$Q_{c,RC} = m_{RC} C_{p,RC} (T_{final} - T_{initial}) \tag{17}$$

$$Q_{c,cont} = m_{cont} C_{p,cont} (T_{final} - T_{initial}) \tag{18}$$

Here, $Q_{c,PCM}$, $Q_{c,RC}$ and $Q_{c,cont}$ are the theoretical amount of heat absorbed by the PCM, RC and metallic container during the charging process, respectively, $Q_{sens,c,s}$ and $Q_{sens,c,l}$ are the theoretical amount of sensible heat absorbed by the PCM in solid and liquid phase during the charging process, respectively, $Q_{lat}$ is the theoretical amount of latent heat absorbed by the PCM during the charging process, $m_{PCM}$, $m_{RC}$ and $m_{cont}$ are the mass of the PCM, RC and metallic container, $C_{p.PCM}$, $C_{p.RC}$ and $C_{p.cont}$ are the specific heat capacity of the PCM, RC and metallic container, $L_{PCM}$ is the PCM latent heat of fusion, $T_{melt,lower}$ and $T_{melt,higher}$ are the starting and ending temperatures of the PCM melting process

(equal to 41 °C and 44 °C, respectively), $T_{initial}$ and $T_{final}$ are the initial and final temperatures for the calculation of the LHTESS thermal performance (equal to 36 °C and 48 °C, respectively).

Similarly, the theoretical heat-release capability of the LHTESS during the discharging process ($Q_{d,th}$) can be assessed according to Eqs. (19)–(26):

$$Q_{d,loss} = Q_{d,th} - Q_d \tag{19}$$

$$Q_{d,th} = \begin{cases} Q_{d,PCM} + Q_{d,cont} & \text{for configuration RP} \\ Q_{d,PCM} + Q_{d,RC} + Q_{d,cont} & \text{for configurations C1, C2, C3} \end{cases} \tag{20}$$

$$Q_{d,PCM} = Q_{sens,d,l} + Q_{lat} + Q_{sens,d,s} \tag{21}$$

$$Q_{sens,d,l} = m_{PCM} C_{p,PCM} \left(T_{final} - T_{melt,higher}\right) \tag{22}$$

$$Q_{lat} = m_{PCM} L_{PCM} \tag{23}$$

$$Q_{sens,d,s} = m_{PCM} C_{p,PCM} \left(T_{melt,lower} - T_{initial}\right) \tag{24}$$

$$Q_{d,RC} = m_{RC} C_{p,RC} \left(T_{final} - T_{initial}\right) \tag{25}$$

$$Q_{d,cont} = m_{cont} C_{p,cont} \left(T_{final} - T_{initial}\right) \tag{26}$$

$Q_{d,PCM}$, $Q_{d,RC,}$ and $Q_{d,con}$ are the theoretical amounts of heat released by the PCM, RC, and metallic container during the discharging process, respectively, and $Q_{sens,d,l}$ and $Q_{sens,d,s}$ are the theoretical amounts of sensible heat released by the PCM in liquid and solid phase during the discharging process, respectively. All other variables are the same as defined for the charging cycle. It is worth mentioning that the values of effective and theoretical heat released by the PCM, RC and metallic container during the discharging process are calculated as positive according to the previous Equations.

This study also utilizes the Ragone plot to compare the thermal performance of the different LHTESS configurations. The Ragone plot is commonly used to assess energy and power densities in energy storage systems, such as lithium-ion batteries [62–64]. On the other hand, using a Ragone plot to assess LHTESS thermal performance is challenging due to the specific nature of PCMs. Energy density depends on factors such as latent heat and subcooling, while the heat-storing material thermal conductivity, HTF operating conditions and system design influence power density. PCMs operate within narrow temperature ranges, and challenges such as low thermal conductivity, scaling effects, and material degradation complicate standardized evaluations [65,66].

Despite the issues mentioned above, several researchers addressed these limitations by using the average or specific point temperature as a comparison criterion. For instance, Woods et al. [67] used the plot to examine the impact of PCM thickness within a LHTESS. Lin et al. [68] applied the same methodology to evaluate the thermal performance of a PCM-based heat battery for granular heat-storage materials, such as RC mixed with PCM.

To summarize, this paper developed a Ragone plot based on volumetric energy density and volumetric power density to clearly compare LHTESS performance across materials with different compositions. Volumetric energy density is obtained from the stored and released energy, while volumetric power density is determined using the duration of the charging or discharging process, as described in Eqs. (27)–(30).

$$Q_{v,c} = \frac{Q_c}{V} \tag{27}$$

$$Q_{v,d} = \frac{Q_d}{V} \tag{28}$$

$$P_{v,c} = \frac{Q_c}{V t_c} \tag{29}$$

$$P_{v,d} = \frac{Q_d}{V t_d} \tag{30}$$

Here, $Q_{v,c}$ and $Q_{v,d}$ represent the volumetric energy density of the LHTESS during the charging and discharging processes, respectively, and $P_{v,c}$ and $P_{v,d}$ correspond to the volumetric power density of the charging and discharging processes. In addition, $V$ is the volume of the storage container, equal to 2835 $cm^3$, and $t_c$ and $t_d$ represent the durations of the charging and discharging processes, respectively. $t_c$ and $t_d$ are calculated as the difference between $t_{end,c}$ and $t_{start,c}$, and $t_{end,d}$ and $t_{start,d}$, respectively.

In this work, $Q_c$ represents the thermal energy absorbed during the charging process, while $Q_d$ represents the thermal energy released during the discharging process. Both quantities are treated as positive magnitudes for consistency and are directly used in the calculation of volumetric energy and power densities in the Ragone analysis for charging and discharging modes, respectively.

## 3. Results and discussion

### 3.1. RC chemical and physical properties

Typically, packing void fraction and bulk density are inversely related, and a higher void fraction generally corresponds to lower bulk density because more void spaces reduce the mass per unit volume. Nevertheless, when dealing with RC, the relationship between void fraction and bulk density can differ from that of natural aggregates or virgin concrete, due to the crushing and processing of old concrete, which results in irregularly shaped aggregates. Additionally, some components exhibit higher physical resistance, making their distribution unpredictable relative to the dedicated sieving sizes. For example, the residual mortar attached to aggregates can influence the bulk density relationship.

Table 5 presents the packing void fractions and bulk densities for the RC types considered in this paper, as assessed experimentally, along with their corresponding relative experimental uncertainties. Reported data highlight that RC with grain size equal to 1–1.7 mm (category B) has the highest bulk density with 1.3890 g/$cm^3$, followed by category C (grain diameter of 1.7–2.36 mm) and category A (grain size equal to 0.6–1 mm) with 1.3265 g/$cm^3$ and 1.271 g/$cm^3$, respectively. The gravimetric impregnation test showed a consistent mass increase from 10 g to approximately 10.3 g for all RC fractions (C1, C2, and C3), corresponding to a PCM uptake of about 3 wt% (±0.1). No significant differences in PCM uptake were observed among the RC fractions under the applied impregnation conditions.

On the other hand, the RC categories present a different trend in void fraction. Category C registered the highest figure, equal to about 47%, almost 2% higher than type B (45.16%). Finally, the RC characterized by the finest grain (category A), presented the lowest void fraction, equal to 44.80%.

From the graphs provided by the MIRA 3 device (Fig. 5), Oxygen (O) is the dominant element in the selected RC compounds, with a concentration exceeding 50%. It is worth mentioning that the RC with the smallest grain size has the highest Oxygen concentration, equal to 52.17%. Calcium (Ca) is another common element in recycled concrete. The experimental measures show that the higher the RC grain diameter, the higher the Calcium share. By scaling from the coarse RC category C

**Table 5**
Bulk density and packing void fraction of RC categories.

| RC category (grain size) | A (0.6–1 mm) | B (1–1.7 mm) | C (1.7–2.36 mm) |
|---|---|---|---|
| Average bulk density (g/$cm^3$) (± 1%) | 1.2710 | 1.3890 | 1.3265 |
| Average packing void fraction (%) (± 1%) | 44.80 | 45.16 | 46.98 |

to the most fine category A, the Calcium proportion decreases from 33% to 19.84%. On the contrary, the Carbon (C) share decreases with increasing grain size, with concentrations of 13.03%, 11.18%, and 9.08% for categories A, B, and C, respectively. Silica (Si) is the next notable constituent, with a concentration ranging from 5% to 10%. In addition, the RC compounds are based on other chemical substances with shares of less than 4%, including magnesium (Mg), aluminum (Al), and iron (Fe). Generally, both Calcium and Silica (Si) contribute to the thermal performance of RC-PCM mixtures used in storage systems, with Calcium having the most significant impact. The surface morphology and structural differences were observed at 154× magnification, and further test specifications are detailed in Fig. 4. Due to the high magnification, the edges of the coarse sample C fell outside the camera's field of view, explaining their absence in the images. In contrast, the smaller grain-size samples A and B fit within the frame and are clearly visible for comparison.

Concrete is made of water, cement, and fine and coarse aggregates (see Table 2). Aggregates and cement paste have different crushing resistances and densities. During the crushing process, the concentration of aggregates, usually made of Calcium-rich stones, remains high because they resist being broken down. Conversely, cement paste rich in Carbon, Oxygen, and Silica breaks down into finer particles more easily. Therefore, the deviation from the expected density of the RC categories is due to compositional balance rather than grain size. More in detail, each component has a different density, which can affect the total bulk density of the RC compound.

According to Fig. 5, the RC category B is denser than the other compounds due to its highest silicon content, which is almost equal to 11.00% by mass, contributing significantly to the total bulk density. It also maintains a moderate concentration of Calcium and Carbon, equal to 20.90% and 11.18%, respectively, minimizing the negative impact of lighter materials. It is worth mentioning that the data reported in Fig. 5 derive from surface composition measurements, obtained through the SEM-EDS technique.

### 3.2. Experimental results on the LHTESS thermal performance

The LHTESS thermal performance during the charging process was assessed by calculating the charging thermal power. It represents the instantaneous heat transfer rate between the HTF stream and the heat-storing material, providing insight into the system heat transfer efficiency. In Fig. 6, the LHTESS thermal performance during the charging process is shown as a function of $\Delta T$ for all the studied configurations.

Fig. 6a ($\Delta T = 10$ K) shows that the thermal power is strongly time-dependent, with the most significant contribution occurring during the initial part of the charging process. The RP configuration exhibits the weakest performance, with thermal power decreasing rapidly over time and an average value of 59 W, reflecting limited heat transfer capability.

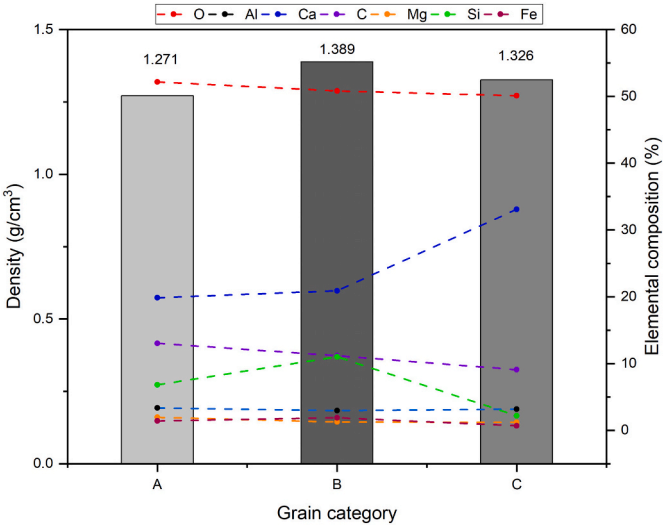


**Fig. 5.** Density (bars) and chemical composition (dashed lines) across RC categories.

In contrast, the addition of recycled concrete particles substantially enhances both peak and average thermal power. Configuration C1 (fine particles) demonstrates the best performance, achieving an average thermal power of 173 W, nearly three times higher than RP. Configurations C2 and C3 show comparable but slightly lower average values (160 W and 158 W, respectively), indicating that increasing particle size reduces heat transfer efficiency. The higher average power of C1 is attributed to the larger contact surface area and improved heat transfer within the PCM matrix, allowing it to sustain higher power for a longer charging duration.

Fig. 6b shows that increasing the inlet temperature difference to 15 K results in a noticeable increase in thermal power across all configurations, particularly during the early charging stage. The average thermal power of RP rises to 89 W, while C1, C2, and C3 reach 231 W, 225 W, and 220 W, respectively. Compared with the lower temperature difference, this corresponds to an increase of approximately 50% for RP and 30–35% for the composite systems. Despite improvements in thermal power and a shorter effective charging time, the performance ranking among the studied configurations remains unchanged. This confirms that while a higher inlet temperature difference intensifies heat transfer, the particle size of recycled concrete remains the dominant factor governing the average thermal power of the LHTESS.

Fig. 7 presents the cumulative thermal energy supplied to the storage unit to raise its temperature from 36 °C to 48 °C at $\Delta T = 10$ K and $\Delta T = 15$ K. It also shows the theoretical stored energy represented in a dashed

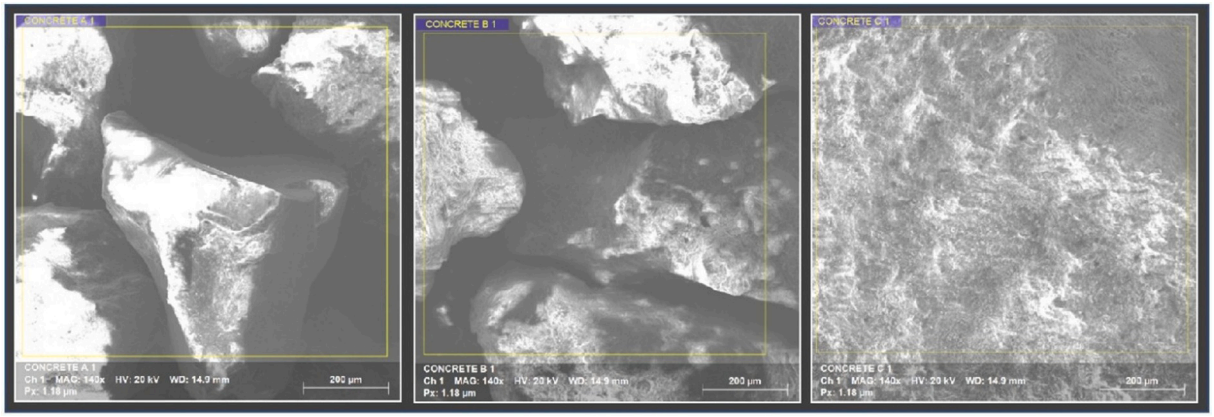


**Fig. 4.** Micrographs of the RC categories A (fine grain), B (medium-size grain) and C (coarse grain) obtained with the SEM analysis.

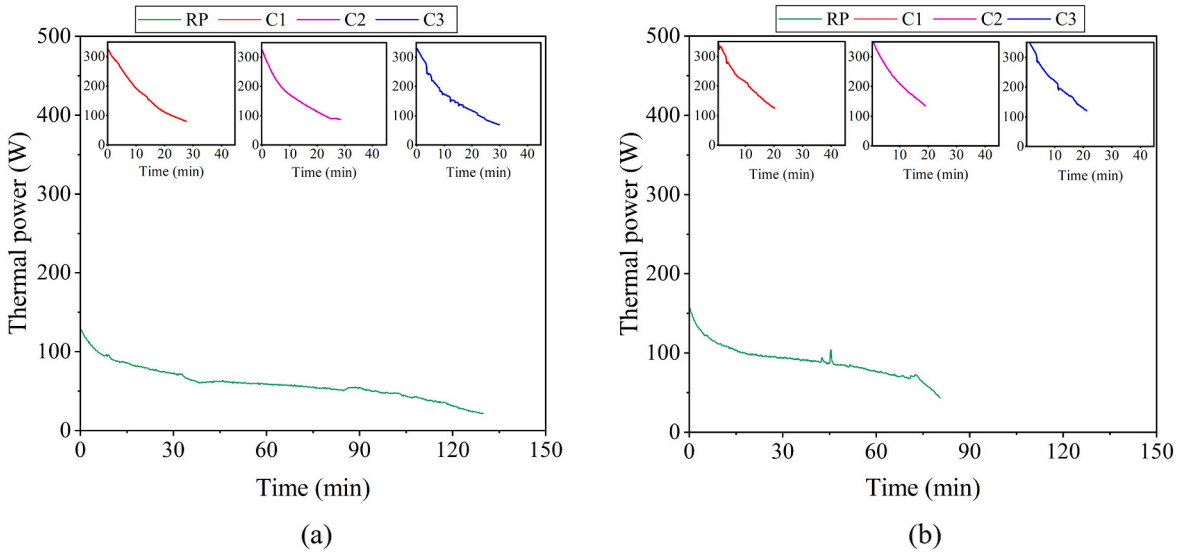


**Fig. 6.** Thermal performance of the LHTESS configurations during the charging process for ΔT = 10 K (a) and ΔT = 15 K (b).

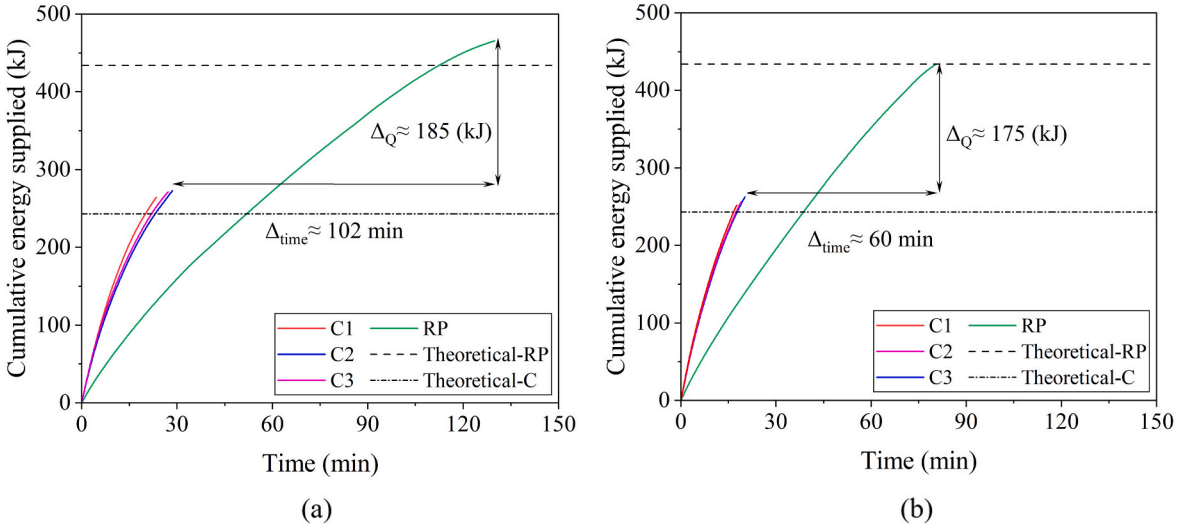


**Fig. 7.** Cumulative thermal energy stored during the LHTESS charging process as a function of heat-storing material for ΔT = 10 K (a) and ΔT = 15 K (b).

line for pure PCM and a short dash-dot line for RC-PCM mixtures. According to Eqs. (11) and (18), the thermal energy theoretically storable by configurations based on RP and RC-PCM compounds is equal to 434 kJ and 243 kJ, respectively. The difference between the cumulative thermal energy supplied to the LHTESS and the aforementioned values is considered a heat loss in charging cycles. The results in Fig. 7a indicate that the RP configuration exhibits a heat loss rate of 6.8% (31 kJ) at $\Delta T$ = 10 K, due to the low heat transfer rate of the pure PCM. In contrast, configurations based on RC-PCM compounds show slightly higher heat loss rates, with C1 at 8.6%, C2 at 9%, and C3 at 10.5%.

More to the point, Fig. 7a indicates that the LHTESS employing pure PCM as the heat-storing material received approximately 465 kJ of heat to reach the target temperature of 48 °C, which is about 60% higher than the systems based on RC-PCM compounds. However, the latter LHTESS configurations had shorter charging times than the reference system using pure PCM. In this case, the system charging process lasted about 132 min, more than 4 times longer than the charging time of the LHTESS using RC-PCM compounds. In particular, the system thermal performance does not vary significantly with the typologies of recycled concrete. The mixture C1 shows the best performance, with a supplied heat of 265 kJ and a charging time of 24 min. The compounds C2 and C3 exhibit a slight increase in cumulative energy input to 285 and 289 kJ, respectively. With these configurations, the charging time is prolonged to 25.5 and 26.5 min, respectively.

A summary of the system thermal performance is presented in Table 6. The findings indicate that increasing $\Delta T$ primarily improves heat-storage performance by accelerating the charging process. For pure

**Table 6**
Thermal performance of the LHTESS configurations during the charging process.

| Configuration | $\Delta T$ (K) | Supplied energy (kJ) | Average thermal power (W) | Process duration (min) | Heat loss (kJ) |
|---|---|---|---|---|---|
| RP | 10 | 465 | 59 | 130 | 31 |
| | 15 | 439 | 89 | 80.5 | 5 |
| C1 | 10 | 265 | 173 | 27.5 | 21 |
| | 15 | 256 | 231 | 20 | 9 |
| C2 | 10 | 285 | 159 | 28.5 | 41 |
| | 15 | 262 | 225 | 20.5 | 18 |
| C3 | 10 | 289 | 158 | 30 | 45 |
| | 15 | 280 | 220 | 21 | 36 |

PCM, the cumulative energy input decreases by approximately 7% as $\Delta T$ increases, while the charging time is reduced by about 39%. This energy demand drop is a consequence of faster heat transfer at higher HTF temperatures, rather than increased system losses. For RC-PCM mixtures, the total delivered energy decreases by an average of around 4% with increasing $\Delta T$, and charging times reduce modestly by about 25%, reflecting a pronounced sensitivity to $\Delta T$ changes. These results show that higher $\Delta T$ primarily shortens charging duration and slightly reduces total energy requirements, with minimal effect on cumulative heat losses.

The comparison of Fig. 7a and b shows that the heat-loss ratio decreases by increasing $\Delta T$ from 10 to 15 K. Reported data indicate that configuration RP exhibits a heat loss ratio equal to 1.2%, while the RC-PCM compounds show higher values: 5% for C1, 7.5% for C2, and 9.5% for C3. These results indicate that a higher HTF inlet temperature leads to reduced overall heat loss, attributed to the shorter charging time at the higher driving temperature.

Regarding the cumulative energy released during the discharging cycles of the LHTESS, the results reported in Fig. 8 indicate that the total discharged energy of the RP configuration was substantially higher than that of the RC-PCM categories. Nevertheless, the released thermal energy in the RP configuration was approximately 18% and 10% lower than the corresponding stored energy at $\Delta T = 10$ K and $\Delta T = 15$ K, respectively. This discrepancy may be associated with a combination of thermophysical and system-level effects. In particular, subcooling during solidification and phase-change hysteresis may limit complete latent heat recovery. These mechanisms are discussed here as plausible contributors rather than being directly quantified in the present experiments. Moreover, the discharging process of RP was 40% faster than the charging duration.

In contrast, the cumulative released energy of the RC-PCM components remained within a similar range to that observed during charging, exhibiting approximately a 15% shorter discharging duration. Among all configurations, the LHTESS based on configuration C1 demonstrated a slightly superior thermal release performance, as illustrated in Fig. 8.

The Ragone plots describing the LHTESS thermal performance during the charging and discharging processes are shown in Fig. 9. The experimental results for charging cycles (see Fig. 9a) show that using a mixture of RC and PCM as a heat-storing material decreases the energy density by approximately 55% compared to a pure PCM configuration, due to the reduced PCM amount (from 1.57 kg in configuration RP to 0.71 kg in configurations C1-C3). On the other hand, RC-PCM matrices increased the power density by approximately a factor of three, reaching about 90 kW/m$^3$ at $\Delta T = 10$ K and 130 kW/m$^3$ at $\Delta T = 15$ K, on average. In comparison, the reference PCM (RP) showed lower power densities of 30 kW/m$^3$ at $\Delta T = 10$ K and 45 kW/m$^3$ at $\Delta T = 15$ K. Furthermore, the experimental results indicate that increasing the HTF inlet temperature during the charging process significantly influences the volumetric power density of LHTESSs using both RC-PCM and RP, with variations of about 50%.

A comparison of the Ragone plots reporting the LHTESS thermal performance during charging and discharging cycles shows that the volumetric energy density of the RP configuration decreased by 17% at $\Delta T = 10$ K and by 10% at $\Delta T = 15$ K during the heat-releasing process. The results also demonstrate that the power density increased by 30% and 45% during discharging cycles, respectively. In contrast, the RC-PCM compounds exhibited only minor changes of around 2% in both energy and power density during charging and discharging.

In order to clearly show the LHTESS performance figures, the volumetric energy and power density values are reported in Table 7 for all studied configurations. The comparison of the LHTESS thermal performance among the RC-PCM configurations revealed only minor differences. However, compound C1 consistently achieved the highest storage capacity and average heat transfer rate, making it the most effective configuration. Moreover, the results indicate that incorporating RC into PCM reduces the overall energy storage density by approximately 55% compared to pure PCM. However, this drawback is compensated by a substantial improvement in the system thermal performance, with the RC–PCM compound achieving nearly 300% higher thermal power during charging/discharging cycles. The reduced energy density can be offset by increasing the storage volume while benefiting from faster thermal response and improved power delivery.

Furthermore, an RC–PCM storage would need to be approximately 40% larger to obtain the same amount of stored heat as a pure PCM-based system. The additional volume is primarily filled with recycled concrete, a low-cost, sustainable material; therefore, the difference lies only in the increased casing and tubing requirements. This trade-off makes RC–PCM a promising solution for designing cost-effective, sustainable, and high-performance latent heat thermal energy storage systems.

## 4. Conclusions

In the present study, we investigated the thermal performance of a Latent Heat Thermal Energy Storage System (LHTESS) utilizing different heat-storing materials. The system consists of a single-row copper tube, in which the Heat Transfer Fluid (HTF) flows, placed within a metallic container filled with the storage material. Two configurations of the

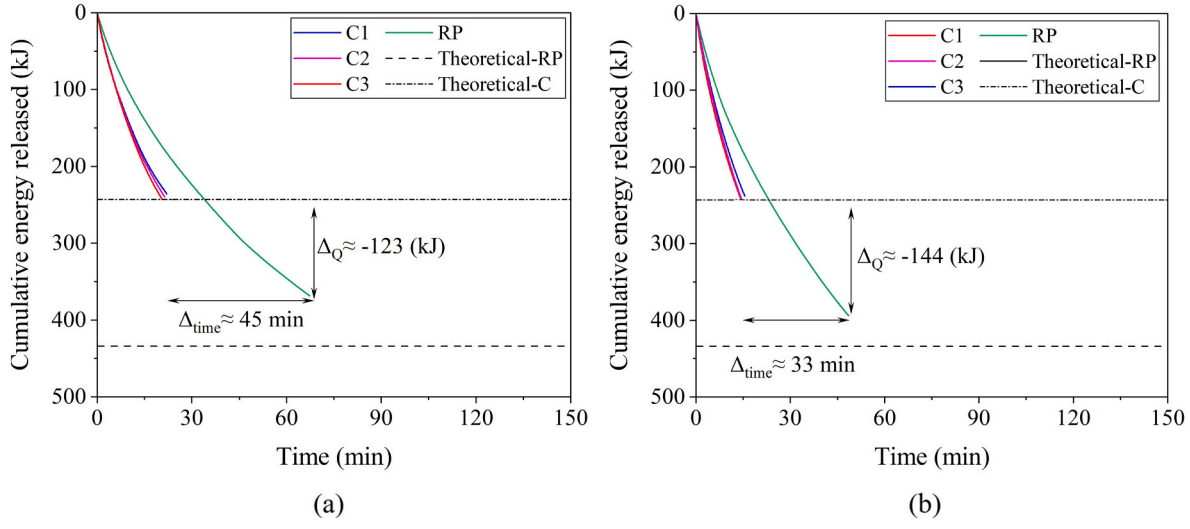


**Fig. 8.** Cumulative thermal energy released during the LHTESS discharging process as a function of heat-storing material for ΔT = 10 K (a) and ΔT = 15 K (b).

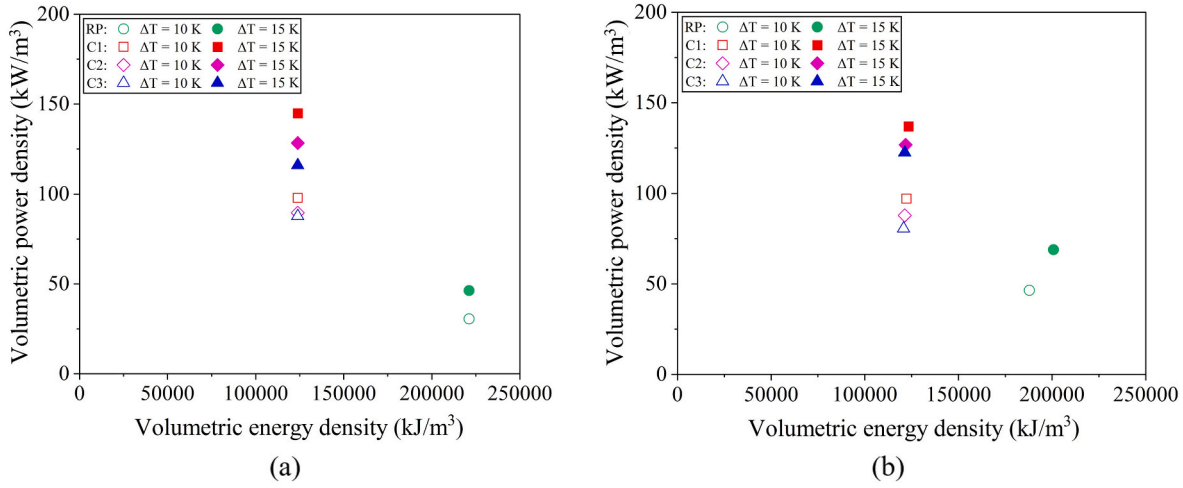


**Fig. 9.** Ragone plots of the LHTESS thermal performance for the charging (a) and discharging (b) processes as a function of ΔT and heat-storing material.

**Table 7**
Volumetric power and energy density of RP, C1, C2, C3, in charging and discharging cycles.

| Configuration | Process | $\Delta T$ (K) | Volumetric power density (kW/m$^3$) | Volumetric energy density (kJ/m$^3$) |
|---|---|---|---|---|
| RP | Charging | 10 | 28 | 221,166 |
| | | 15 | 45 | 221,166 |
| | Discharging | 10 | 46 | 187,748 |
| | | 15 | 68 | 200,681 |
| C1 | Charging | 10 | 89 | 123,943 |
| | | 15 | 137 | 123,943 |
| | Discharging | 10 | 97 | 122,292 |
| | | 15 | 137 | 123,312 |
| C2 | Charging | 10 | 76 | 123,943 |
| | | 15 | 119 | 123,943 |
| | Discharging | 10 | 87 | 121,273 |
| | | 15 | 126 | 121,783 |
| C3 | Charging | 10 | 73 | 123,943 |
| | | 15 | 100 | 123,943 |
| | Discharging | 10 | 80 | 120,764 |
| | | 15 | 122 | 121,273 |

LHTESS were tested during charging and discharging cycles using water as the HTF. The commercial paraffinic Phase Change Material (PCM) RT-44HC was used as reference heat-storing material (configuration RP). Different Recycled Concrete (RC) and PCM mixtures, with weighting ratios of 79.3% and 20.7%, were used as heat-storing media to improve the system thermal performance. Three types of RC, characterized by grain diameters ranging from 0.6 to 2.36 mm, were considered (configurations C1, C2 and C3).

The chemical and physical properties of RC mixtures were evaluated using SEM analysis. The results indicate that RC density is more influenced by chemical composition than by grain size, as cement acts as a binding agent in concrete. Then, the LHTESS thermal performance was assessed as a function of the heat-storing material and the HTF operating conditions.

The use of RC–PCM as a heat-storing material in LHTESSs reduced the measured storage capacity by approximately 40% compared to a system using pure PCM, while charging and discharging times decreased by up to 75% in the tested RC–PCM configurations. The HTF inlet conditions significantly affected the observed thermal performance during both charging and discharging cycles, with a stronger effect in pure PCM systems than in RC–PCM systems. Increasing the HTF inlet temperature reduced the energy density during charging cycles and increased it during discharging cycles. The adoption of RC–PCM compounds reduced the amount of pure PCM required by about 50%, lowering environmental impacts. While measured performance differences among RC–PCM configurations were small, configuration C1 showed slightly higher effectiveness, which may be associated with its lower void fraction.

The results of this study can support the design of compact LHTESSs, which require higher thermal performance and, thus, faster charging and discharging cycles. Using an RC–PCM mixture eliminates the need for metallic inserts typically used in latent TES systems based on pure PCMs, thereby lowering capital and operational costs. Furthermore, incorporating recycled concrete enhances sustainability by repurposing waste materials and improving resource efficiency. The findings of this work are specific to the recycled railway-sleeper concrete examined, and no generalization to other concrete types is intended. Future studies should include detailed material-property characterization, such as void fraction, PCM uptake, and thermal properties, including thermal diffusivity of the RC–PCM matrix, to enable reliable evaluation of non-dimensional parameters (i.e., Nusselt, Stefan, and Rayleigh numbers). This would also allow a clearer assessment of the effects of particle size and composition on the system thermal performance and would generalize the obtained findings. Further work could explore alternative PCMs or hybrid composites to improve the LHTESS energy density, while also incorporating life-cycle assessment and cost analysis to evaluate sustainability and economic feasibility. Finally, larger-scale testing and long-term cycling studies are recommended to assess practical performance and durability in real thermal energy storage applications.

## CRediT authorship contribution statement

**Fardin Jafari:** Writing – review & editing, Visualization, Validation, Resources, Project administration, Methodology, Investigation, Formal analysis, Data curation. **Matteo Dongellini:** Writing – review & editing, Visualization, Validation, Supervision, Project administration, Methodology, Formal analysis. **Giovanni Semprini:** Validation, Supervision, Project administration, Methodology, Investigation. **Gabriella Adele D'Errico:** Project administration, Methodology. **Alessandra Bonoli:** Supervision, Project administration, Methodology.

## Declaration of competing interest

The authors declare that they have no known competing financial interests or personal relationships that could have appeared to influence the work reported in this paper.

## Acknowledgments

The authors sincerely thank Maurizio Chendi, Stefania Falcioni, and

Fabrizio Casarini, laboratory technicians at the Department of Industrial Engineering, University of Bologna, for their valuable support and collaboration during the experimental activities.

## Data availability

Data will be made available on request.

## References


[1] F. Martins, C. Felgueiras, M. Smitkova, N. Caetano, Analysis of fossil fuel energy consumption and environmental impacts in European countries, Energies (Basel) 12 (2019) 964.

[2] S.A. Solarin, An environmental impact assessment of fossil fuel subsidies in emerging and developing economies, Environ. Impact Assess. Rev. 85 (2020) 106443.

[3] A.K. Akella, R.P. Saini, M.P. Sharma, Social, economical and environmental impacts of renewable energy systems, Renew. Energy 34 (2009) 390–396.

[4] C. Prieto, P. Cooper, A.I. Fernández, L.F. Cabeza, Review of technology: thermochemical energy storage for concentrated solar power plants, Renew. Sust. Energ. Rev. 60 (2016) 909–929.

[5] I. Dincer, S. Dost, X. Li, Performance analyses of sensible heat storage systems for thermal applications, Int. J. Energy Res. 21 (1997) 1157–1171.

[6] I. Dincer, On thermal energy storage systems and applications in buildings, Energ. Buildings 34 (2002) 377–388.

[7] A.J. Parry, P.C. Eames, F.B. Agyenim, Modeling of thermal energy storage shell-and-tube heat exchanger, Heat Transf. Eng. 35 (2014) 1–14.

[8] J.P. da Cunha, P. Eames, Compact latent heat storage decarbonisation potential for domestic hot water and space heating applications in the UK, Appl. Therm. Eng. 134 (2018) 396–406.

[9] J.P. Da Cunha, P. Eames, Thermal energy storage for low and medium temperature applications using phase change materials–a review, Appl. Energy 177 (2016) 227–238.

[10] M. Fadl, P.C. Eames, A comparative study of the effect of varying wall heat flux on melting characteristics of phase change material RT44HC in rectangular test cells, Int. J. Heat Mass Transf. 141 (2019) 731–747.

[11] M.M. Farid, A.M. Khudhair, S.A.K. Razack, S. Al-Hallaj, A review on phase change energy storage: materials and applications, Energy Convers. Manag. 45 (2004) 1597–1615.

[12] N.H.S. Tay, M. Belusko, F. Bruno, An effectiveness-NTU technique for characterising tube-in-tank phase change thermal energy storage systems, Appl. Energy 91 (2012) 309–319.

[13] G. Dogkas, J. Konstantaras, M.K. Koukou, M.G. Vrachopoulos, C. Pagkalos, V. N. Stathopoulos, P.K. Pandis, K. Lymperis, L. Coelho, A. Rebola, Development and experimental testing of a compact thermal energy storage tank using paraffin targeting domestic hot water production needs, Therm. Sci. Eng. Prog. 19 (2020) 100573.

[14] H. Wang, H. Xu, C. Liu, Z. Zhang, X. Ling, F. Jiang, Numerical investigation of melting enhancement for paraffin in an innovative finned-plate latent heat thermal energy storage unit, J. Energy Storage 43 (2021) 103222.

[15] C. Zhao, J. Wang, Y. Sun, S. He, K. Hooman, Fin design optimization to enhance PCM melting rate inside a rectangular enclosure, Appl. Energy 321 (2022) 119368.

[16] C. Zhao, M. Opolot, M. Liu, F. Bruno, S. Mancin, K. Hooman, Numerical study of melting performance enhancement for PCM in an annular enclosure with internal-external fins and metal foams, Int. J. Heat Mass Transf. 150 (2020) 119348.

[17] B. Kamkari, H. Shokouhmand, Experimental investigation of phase change material melting in rectangular enclosures with horizontal partial fins, Int. J. Heat Mass Transf. 78 (2014) 839–851.

[18] N. Sharifi, T.L. Bergman, A. Faghri, Enhancement of PCM melting in enclosures with horizontally-finned internal surfaces, Int. J. Heat Mass Transf. 54 (2011) 4182–4192.

[19] V. Shatikian, G. Ziskind, R. Letan, Numerical investigation of a PCM-based heat sink with internal fins, Int. J. Heat Mass Transf. 48 (2005) 3689–3706.

[20] M. Lacroix, M. Benmadda, Analysis of natural convection melting from a heated wall with vertically oriented fins, Int. J. Numer. Methods Heat Fluid Flow 8 (1998) 465–478.

[21] A. Abdi, M. Shahrooz, J.N.W. Chiu, V. Martin, Experimental investigation of solidification and melting in a vertically finned cavity, Appl. Therm. Eng. 198 (2021) 117459.

[22] P. Lamberg, K. Siren, Analytical model for melting in a semi-infinite PCM storage with an internal fin, Heat Mass Transf. 39 (2003) 167–176.

[23] C. Ji, Z. Qin, S. Dubey, F.H. Choo, F. Duan, Simulation on PCM melting enhancement with double-fin length arrangements in a rectangular enclosure induced by natural convection, Int. J. Heat Mass Transf. 127 (2018) 255–265.

[24] S. Mat, A.A. Al-Abidi, K. Sopian, M.Y. Sulaiman, A.T. Mohammad, Enhance heat transfer for PCM melting in triplex tube with internal–external fins, Energy Convers. Manag. 74 (2013) 223–236.

[25] M. Lacroix, M. Benmadda, Numerical simulation of natural convection-dominated melting and solidification from a finned vertical wall, Numeri. Heat Transf. A Appl. 31 (1997) 71–86.

[26] Z.N. Meng, P. Zhang, Experimental and numerical investigation of a tube-in-tank latent thermal energy storage unit using composite PCM, Appl. Energy 190 (2017) 524–539.

[27] G. Ferrer, A. Solé, C. Barreneche, I. Martorell, L.F. Cabeza, Corrosion of metal containers for use in PCM energy storage, Renew. Energy 76 (2015) 465–469.

[28] O.M. Adesusi, O.R. Adetunji, S.I. Kuye, A.I. Musa, T.J. Erinle, O.B. Gbadamosi-Olatunde, S.O. Ipadeola, A comprehensive review of the materials degradation phenomena in solid-liquid phase change materials for thermal energy storage, Int. J. Thermofluids 18 (2023) 100360.

[29] W. Hua, X. Xu, X. Zhang, H. Yan, J. Zhang, Progress in corrosion and anti-corrosion measures of phase change materials in thermal storage and management systems, J. Energy Storage 56 (2022) 105883.

[30] A. Vasu, F.Y. Hagos, M.M. Noor, R. Mamat, W.H. Azmi, A.A. Abdullah, T. K. Ibrahim, Corrosion effect of phase change materials in solar thermal energy storage application, Renew. Sust. Energ. Rev. 76 (2017) 19–33.

[31] S. Singh, K. Sørensen, T. Condra, Investigation of material efficient fin patterns for cost-effective operation of fin and tube heat exchanger, Appl. Therm. Eng. 126 (2017) 903–914.

[32] H. Najafi, B. Najafi, P. Hoseinpoori, Energy and cost optimization of a plate and fin heat exchanger using genetic algorithm, Appl. Therm. Eng. 31 (2011) 1839–1847.

[33] L.F. Cabeza, C. Castellón, M. Nogués, M. Medrano, R. Leppers, O. Zubillaga, Use of microencapsulated PCM in concrete walls for energy savings, Energ. Buildings 39 (2007) 113–119.

[34] Y. Shen, S. Liu, C. Zeng, Y. Zhang, Y. Li, X. Han, L. Yang, X. Yang, Experimental thermal study of a new PCM-concrete thermal storage block (PCM-CTSB), Constr. Build. Mater. 293 (2021) 123540.

[35] D. Niall, O. Kinnane, R.P. West, S. McCormack, Mechanical and thermal evaluation of different types of PCM–concrete composite panels, J. Struct. Integr. Maint. 2 (2017) 100–108.

[36] S. Dora, F. Kuznik, K.M. Mini, A novel PCM-based foam concrete for heat transfer in buildings-experimental developments and simulation modelling, J. Energy Storage 105 (2025) 114625.

[37] N. Serres, S. Braymand, F. Feugeas, Environmental evaluation of concrete made from recycled concrete aggregate implementing life cycle assessment, J. Build. Eng. 5 (2016) 24–33.

[38] S. Barbhuiya, B.B. Das, M. Idrees, Thermal energy storage in concrete: A comprehensive review on fundamentals, technology and sustainability, J. Build. Eng. 82 (2024) 108302.

[39] N. Madeswaran, F.J. Desai, E. Asmatulu, Life cycle inventory and performance analysis of phase change materials for thermal energy storages, Emerg. Mater. 4 (2021) 1697–1709.

[40] B. Nienborg, S. Gschwander, G. Munz, D. Fröhlich, T. Helling, R. Horn, H. Weinläder, F. Klinker, P. Schossig, Life cycle assessment of thermal energy storage materials and components, Energy Procedia 155 (2018) 111–120.

[41] Rubitherm Technologies GmbH, Techdata – RT44HC, Berlin, Germany, 2025. https://www.rubitherm.eu/en/productcategory/organische-pcm-rt (accessed August 12, 2025).

[42] W. Ferdous, A. Manalo, Failures of mainline railway sleepers and suggested remedies–review of current practice, Eng. Fail. Anal. 44 (2014) 17–35.

[43] N.Ö. Bezgin, High performance concrete requirements for prefabricated high speed railway sleepers, Constr. Build. Mater. 138 (2017) 340–351.

[44] B. Xu, J. Han, A. Kumar, P. Li, Y. Yang, Thermal storage using sand saturated by thermal-conductive fluid and comparison with the use of concrete, J. Energy Storage 13 (2017) 85–95.

[45] N. Bagdassarov, N. Bagdassarov, Fundamentals of Rock Physics, Cambridge University Press, 2021.

[46] F.G.A. Verheijen, A. Zhuravel, F.C. Silva, A. Amaro, M. Ben-Hur, J.J. Keizer, The influence of biochar particle size and concentration on bulk density and maximum water holding capacity of sandy vs sandy loam soil in a column experiment, Geoderma 347 (2019) 194–202.

[47] Y. Yan, L. Zhang, X. Luo, C. Li, F. Hu, A new method for calculating the primary porosity of unconsolidated sands based on packing texture: application to modern beach sand, Mar. Pet. Geol. 98 (2018) 384–396.

[49] U. Berardi, M. Naldi, The impact of the temperature dependent thermal conductivity of insulating materials on the effective building envelope performance, Energ. Buildings 144 (2017) 262–275, https://doi.org/10.1016/J.ENBUILD.2017.03.052.

[51] M. Fadl, P.C. Eames, An experimental investigation of the heat transfer and energy storage characteristics of a compact latent heat thermal energy storage system for domestic hot water applications, Energy 188 (2019) 116083.

[52] K. Tofani, S. Tiari, Nano-enhanced phase change materials in latent heat thermal energy storage systems: a review, Energies (Basel) 14 (2021) 3821.

[53] T. Ambreen, H. Niyas, P. Kanti, H.M. Ali, C.-W. Park, Experimental investigation on the performance of RT-44HC-nickel foam-based heat sinks for thermal management of electronic gadgets, Int. J. Heat Mass Transf. 188 (2022) 122591.

[54] F. Jafari, G. Semprini, A. Bonoli, A. Purandare, M. Shahi, Effect of recycled ceramic particle size on heat transfer and charging dynamics in PCM-based thermal storage systems, Appl. Therm. Eng. 288 (2026) 129686, https://doi.org/10.1016/j.applthermaleng.2025.129686.

[55] D.S. Smith, A. Alzina, J. Bourret, B. Nait-Ali, F. Pennec, N. Tessier-Doyen, K. Otsu, H. Matsubara, P. Elser, U.T. Gonzenbach, Thermal conductivity of porous materials, J. Mater. Res. 28 (2013) 2260–2272, https://doi.org/10.1557/JMR.2013.179.

[56] Z.X. Chen, X.X. Guo, L.T. Shao, S.Q. Li, On determination method of thermal conductivity of soil solid material, Soils Found. 60 (2020) 218–228, https://doi.org/10.1016/J.SANDF.2020.03.001.

[57] B.O. Hardin, The nature of damping in sands, J. Soil Mech. Found. Div. 91 (1965) 63–97, https://doi.org/10.1061/JSFEAQ.0000706.

[58] X. Zhang, X. Liu, R. An, C.N. Debeleac, A. Buraga, S.M. Nastac, Experimental and numerical study in dynamic compaction of weakly-cohesive soils, Appl. Sci. 14 (2024) 10129, https://doi.org/10.3390/APP142210129.
[59] M. Dongellini, G. Martino, C. Naldi, S. Lorente, G.L. Morini, Experimental study on the heat transfer performance of finned-tube heat exchangers in latent thermal energy storages: effects of PCM types and operating conditions, Appl. Therm. Eng. 271 (2025) 126273, https://doi.org/10.1016/j.applthermaleng.2025.126273.
[60] M. Zhang, W. Miao, Y. Li, H. Xie, S. Zhu, Correction for Nusselt number correlations of transcritical methane based on radial velocity distribution, Heat Transfer Eng. 46 (2025) 975–988, https://doi.org/10.1080/01457632.2024.2355839.
[62] S.K. Kumar, A.A.B.M. Abduh, O. Sabih, R. Yazami, Temperature effect on "Ragone plots" of lithium-ion batteries, J. Electrochem. Soc. 165 (2018) A674–A679, https://doi.org/10.1149/2.0591803JES/XML.
[63] I. Beyers, A. Bensmann, R. Hanke-Rauschenbach, Ragone plots revisited: a review of methodology and application across energy storage technologies, J. Energy Storage 73 (2023) 109097, https://doi.org/10.1016/J.EST.2023.109097.
[64] M. Shi, J. Hu, H. Han, X. Yuan, Design of battery energy storage system based on Ragone curve, in: 2020 4th International Conference on HVDC, HVDC 2020, 2020, pp. 37–40, https://doi.org/10.1109/HVDC50696.2020.9292767.
[65] K. Yazawa, P.J. Shamberger, T.S. Fisher, Ragone relations for thermal energy storage technologies, Front. Mech. Eng. 5 (2019), https://doi.org/10.3389/FMECH.2019.00029.
[66] V.Z. Vargas, L.J. Claros-Marfil, G.F.B. Sandoval, B.H. Rojas, A.G. Santos, F.J. N. González, Experimental assessment of energy storage in microencapsulated paraffin PCM cement mortars, Case Stud. Constr. Mater. 20 (2024) e02959, https://doi.org/10.1016/J.CSCM.2024.E02959.
[67] J. Woods, A. Mahvi, A. Goyal, E. Kozubal, A. Odukomaiya, R. Jackson, Rate capability and Ragone plots for phase change thermal energy storage, Nat. Energy 6 (2021) 295–302.
[68] X.-W. Lin, Z.-F. Zhou, T.-F. Liu, S.-Q. Xue, Y. Liang, L.-F. Zhang, B. Liu, Rate capability and Ragone plots for designing battery thermal management system based on phase change material, J. Energy Storage 74 (2023) 109539.